



PAPER

A compact stereotactic system for image-guided surgical intervention

Aaron E Rusheen^{1,2,3} , Abhijeet S Barath¹ , Abhinav Goyal^{1,2,3}, J Hudson Barnett^{2,3}, Benjamin T Gifford¹, Kevin E Bennet^{1,4,6}, Charles D Blaha¹, Stephan J Goerss^{1,6}, Yoonbae Oh^{1,5} and Kendall H Lee^{1,5,6}

¹ Department of Neurologic Surgery, Mayo Clinic, Rochester, MN, United States of America

² Mayo Clinic Alix School of Medicine, Mayo Clinic, Rochester, MN 55905

³ Medical Scientist Training Program, Mayo Clinic, Rochester, MN 55905

⁴ Division of Engineering, Mayo Clinic, Rochester, MN 55905, United States of America

⁵ Department of Physiology and Biomedical Engineering, Mayo Clinic, Rochester, MN, United States of America

⁶ NaviNetics, Inc, Rochester, MN 55902, United States of America

E-mail: lee.kendall@mayo.edu and oh.yoonbae@mayo.edu

Keywords: stereotaxy, deep brain stimulation, image-guidance, 3D-printing

Supplementary material for this article is available [online](#)

Abstract

Objective. Stereotactic technology enables fine navigation to small structures in the human body. While current stereotactic systems facilitate accurate targeting, they are mechanically cumbersome and limited in scope. Here, we hypothesized that a stereotactic system could be developed with a reduced footprint while maintaining broad targeting capabilities in order to improve versatility in frame placement location and surgical workflow. **Approach.** We designed a stereotactic system around the center-of-arc principle, with mechanical properties that would enable a compact design and ample targeting and trajectory maneuverability. To examine the opportunity for a low-cost rapidly-deployable system we developed two fabrication variants, one using three dimensional (3D)-printing and the other using conventional machining. Mechanical and image-guided accuracies were tested in phantom studies using magnetic resonance imaging (MRI) and computed tomography. Using human cadaver head specimens, we assessed the system's surgical workflow and its ability to reliably and accurately implant electrodes in deep brain stimulation (DBS) surgery. **Main results.** We developed a small $7.7 \times 5.4 \text{ cm}^2$ device platform that rigidly mounts to curvilinear bone and supports the attachment of surgical instrumentation. Attachment of two surgical instruments, an imaging localizer and a compact targeting device, demonstrated successful MRI-guided intervention in phantom studies with a vector error of $1.79 \pm 0.41 \text{ mm}$. Evaluation of the 3D-printed system for DBS surgery confirmed ease of device platform attachment and instrument functionality, as well as demonstrated a surgical targeting accuracy of $1.83 \pm 0.15 \text{ mm}$. In addition, we found the surgical time to be $78.3 \pm 5.4 \text{ min}$ for bilateral electrode implantation. **Significance.** We developed a light and compact stereotactic system whose accuracy is on par with those used clinically. This technology is suitable for clinical translation and its flexibility in positioning will seamlessly expand the capabilities for stereotaxy to treat a wide range of conditions, both within neurosurgery and beyond.

1. Introduction

Accurate targeting is essential for numerous medical interventions, such as diagnostic biopsy, targeted radiotherapy, and, notably, implantation of deep brain stimulation (DBS) electrodes [1–3]. To achieve high accuracy for surgical intervention, stereotactic surgery was developed in the early 1900s and quickly

applied to target brain pathology and nuclei [4–6]. A prominent category of current stereotactic methods utilize a skull-mounted rigid base-frame creating a three-dimensional (3D) coordinate system used to guide surgical intervention [7]. These methods, when combined with brain imaging technology, are routinely used to treat many neurologic disorders [8–11]. With a fast-growing number of eligible patients

and expanding surgical indications, the use of stereotaxy continues to grow and is vital to surgical practice [12, 13].

There are two primary technological paradigms in present use for stereotactic guidance: frame-based (Leksell®, Cosman-Robert-Wells™) and microtargeting systems (Nexframe®, STarFix™, ClearPoint®) [14]. Frame-based systems employ a base-frame that mounts circumferential to the head with fixation pins for rigid securement [7, 15, 16]. Surgical instruments are attached to the base-frame that include an imaging localizer and a targeting device enabling image-guided surgical intervention to a large envelope of coordinates [7, 17–19]. In contrast, microtargeting systems employ a small device with fixed or limited targeting that secures directly to the skull entry site [1]. While studies directly comparing these systems have found non-significant differences in implantation accuracy (Framed: 1.2–3.2 mm, microtargeting: 2.5–3.2 mm), microtargeting platforms have had poor adoption [20–23]. This is due to non-intuitive mechanics as well as targeting and trajectory limitations [24]. In addition, microtargeting platforms have suffered from a lasting perception of inadequacy and thus the majority of neurologic procedures are conducted using frame-based systems [25, 26].

While conventional frame-based systems have been time-tested for safe and accurate targeting, they have limitations. These systems are heavy, often weighing more than 8 lbs (3.63 kg) [27]. The base-frame must be worn throughout the entirety of the surgical procedure, from initial placement in the operating room to surgical intervention. With long surgical times, often while the patient is awake, the cumbersome design causes considerable discomfort [28]. Patients queried for surgical experience report the base-frame's opposed skin-piercing pins to be the most uncomfortable element of surgery, and a deterrent for many patients who are otherwise excellent candidates [28, 29]. In addition, these frames require a well-integrated and experienced team, reducing efficient use of operating room time and resources [26]. Finally, the design principles of current clinical systems limit their use to brain surgery. We designed a novel system to improve the patient and surgeon experience, provide the required precision and accuracy for therapeutic benefit, and expand use of stereotaxy outside of neurologic disorders.

Our novel stereotactic technology combines the advantages of frame-based and microtargeting stereotactic paradigms. To improve patient comfort and facilitate expanded placement locations, we developed a small 7.7×5.4 cm² device platform that mounts to bone. In addition, we developed two instruments to attach to this platform: an imaging localizer enabling image registration, and a compact targeting device with broad targeting and

trajectory capabilities. To allow for low-cost rapid-deployment stereotaxy, we developed two fabrication variants simultaneously: a single use 3D-printed version, and a conventionally machined repeated use version. Our system achieved reliable and robust image-guided surgical accuracy for the implantation of DBS electrodes, on par with clinical systems. This patient-centered delivery system will expand stereotactic capabilities to a wider range of patients and institutions, and can be applied broadly to diagnose and treat systemic diseases in addition to neurological disorders.

2. Materials and methods

2.1. Experimental design

The main goal of this study was to develop a stereotactic system that was low-profile and provided rigid and versatile attachment to bone. The first objective of our study was to assign the working principles of the stereotactic system that would enable a compact design while still allowing large targeting and trajectory capabilities. Our second objective was to examine material compositions and fabrication techniques that would enable movement of various system components with high tolerances. Our third objective was to test the operational mechanics, as well as examine the system's mechanical and image-guided accuracy. Last, our fourth objective was to assess the system's clinical workflow and determine its ability to reliably and accurately be used in a mock-surgical scenario. Human data used for system design was performed in accordance with the Mayo Clinic Institutional Review Board (IRB #: 18-011400). Studies using human specimens were deemed exempt.

$N = 3$ 3D-printed and $n = 1$ Delrin® systems were fabricated for experimentation. Mechanical accuracy and phantom testing were performed with $n = 3$ 3D-printed and $n = 1$ Delrin® systems by $n = 3$ examiners. Mock-surgical testing was performed with $n = 3$ 3D-printed systems in $n = 5$ experiments using $n = 4$ cadaver specimens.

2.2. Stereotactic system design

To develop this new system a number of design criteria were considered, including increased patient comfort, an arc-centered delivery system, and a compact, user-friendly re-attachable device interface. The stereotactic system included a targeting device, and MRI and computed tomography (CT) N-bar localizers that could be individually attached to a novel, MRI-compatible, skull-mounted device platform. The design of the stereotactic system was performed with the aid of Onshape™ (Onshape, Cambridge, MA) and SolidWorks™ (Dassault Systèmes™, Vélizy-Villacoublay, France). 3D-printing was conducted with Ultimaker™ S5 3D Printers (Ultimaker™, Geldermalsen, Netherlands)

using tough polylactic acid. Delrin® (Dupont, Wilmington, DE) fabrication was performed by machinists in Mayo Clinic's Division of Engineering.

2.3. Localizers

The MRI and CT localizers utilized N-Bar fiducials. The localizers had two side plates and one anterior plate. The parallel bars of the 'N' in each plate were positioned 120 mm apart, and the diagonal rod connecting the parallel rods was at a 45° angle. The side plates were placed 190 mm laterally from each other, and the center of the anterior plate 110 mm from the focus of the four parallel rods. This design allowed for existing surgical software to be used for target planning. For visualization in MRI, the N-shaped bars of the MRI localizer contained grooves that were fitted with flexible plastic tubing (2 mm inner diameter) filled with a 2% copper sulfate (CuSO₄) solution in water. For CT visualization, 2 mm diameter copper rods were fashioned.

2.4. Device platform load testing

Testing was performed in the Mayo Clinic Biomechanics Testing Core (Rochester, MN, USA) on a servo-hydraulic test machine with 14.7 kN load capacity (Model 858 miniBionix, MTS Systems Corporation, Eden Prairie, MN, USA) equipped with a 100 lb, uniaxial load cell (Model: 3397-100, Lebow Products, Troy, MI, USA). A proximity laser sensor (Model: optoNCDT1302-20, Micro-Epsilon Messtechnik GmbH & Co. KG, Ortenburg, Germany) was mounted below the device platform to record any motion. All fixtures, including the loading fixture and test block fixation clamps, were designed to be sufficiently rigid such that minimal deflection occurred.

The device platform was mounted to a test block using titanium screws. The 40 mm thick polyurethane foam test block of density 50 lb ft⁻³ (Sawbones, Vashon Island, WA, USA), intended for use for mechanical testing of orthopedics devices, was used and selected due its material properties most closely matching those of skull bone. Custom load fixtures were fabricated to perform this test (figure S2(A)) (available online at stacks.iop.org/JNE/00/00000/mmedia). The fixture consisted of an L-bracket on which an interface plate was mounted equipped with a clamping interface with the test-block. After mounting the device platform to the test block, the test block was clamped to the test fixture using the interface plate clamps. A 15 cm lever arm was mounted to the top of the device platform such that the lever arm was orthogonal to the test-block surface.

The mounted device platform and block were mounted to the test machine via the loading fixtures described above. An axial load perpendicular to the lever arm was applied 123 mm from the test block's surface, creating a torque at the device platform-block interface. With this base setup, two tests were performed. A torque was applied to the block which

replicated the worst-case-scenario situation in such a way that the torque on the device platform generated by gravity acting on the attached stereotactic targeting device was at its maximum. This resulted in a torque of 1.57 Nm at 1× load, and 4.71 Nm at 3× load. To generate this torque, a downward-directed axial load was applied at a constant displacement of 5 mm min⁻¹ rate until the force generating the desired torque was reached. This position was then held for 10 s and the load was removed by returning the actuator head to its starting position. The applied load (used to compute the applied torque) and displacement of the device platform were recorded. Tests at 1x and 3x load were performed three times in both the anterior and posterior loading conditions.

2.5. Clinical DBS targeting data analysis

DICOM images of 100 DBS patients were obtained from the Department of Radiology and deidentified in accordance with the Mayo Clinic Institutional Review Board (IRB #18-011400). All MRI coordinates were co-registered to that of the first patient using the Statistical Parametric Mapping (SPM) Matlab toolbox. Specifically, each patient's DICOM files were first converted into NIFTI format and then fed into SPM's estimate and reslice coregistration algorithm. Normalized mutual information was used as the objective function, with a [4 2] separation, [7 7] histogram smoothing, and using a 4th degree B-spline as the interpolation function. A transformation matrix was used to determine the coregistered X, Y, and Z entry and target coordinates for each patient relative to patient 1. A Mayavi Python package was used to create a 3D heatmap from these coordinates.

2.6. Mechanical accuracy testing

To assess the mechanical accuracy of the stereotactic system, an aluminum testing device was built in-house that contained 5 points of known coordinates that are accurate to 1/1000 of an inch (25.4 μm). These points, in reference to the targeting device, lie at locations providing a wide coverage of the work envelope. The frame was mounted to the testing device and a 150 mm targeting probe was secured to the targeting device delivery platform. The collar was fixed at 75° and the arc at 90°. The frame was dialed in to target each one of the 5 points with the tip of the probe, and the frame X, Y, and Z coordinate readout compared against the true coordinates of the point to determine the 3D Euclidean error (vector or target error). 3D distances were calculated using the 3D Euclidean distance equation:

$$D = \sqrt{(X_O - X_E)^2 + (Y_O - Y_E)^2 + (Z_O - Z_E)^2}$$

O and E subscripts represent observed and expected values for each linear coordinate. Radial error

was determined as the 2D Euclidean error using the X and Y components. The process of targeting test points was repeated by three independent examiners to account for inter-user variance. All data are presented as mean \pm standard error of the mean (SEM).

2.7. Phantom testing

A customized MRI- and CT-compatible phantom was designed and 3D-printed to evaluate the accuracy and repeatability of the re-attachable stereotactic frame system with MRI and CT imaging. The test phantom included 35 pointed cylindrical targets, which reside at locations providing a wide coverage of the work envelope. MRI and CT images of the phantom were acquired with their respective localizers mounted to the phantom platform. Stereotactic planning software (COMPASSTM, Rochester, MN) was used for image registration and to calculate the Euclidean coordinates at the top center of each cylindrical target. A series of 8 phantom points were targeted with the stereotactic system using the 150 mm probe. The probe was adjusted to touch the top center of each phantom point and the X , Y , and Z values on the frame recorded. The process of targeting phantom points was repeated by three independent examiners to account for inter-user variance. The 3D Euclidean distance between the mechanically targeted and MRI and CT targeted coordinates was calculated to determine how imaging contributed to targeting accuracy. Finally, to assess the error contributed from collar and arc torque, as well as inaccuracies in the collar and arc curvature, the collar and arc were adjusted at 10° increments from one extreme end to the other. At each increment, targeting experiments were performed as described above and the vector and radial errors determined.

2.8. Human cadaver testing

An MRI-guided mock-DBS surgical procedure using the 3D-printed stereotactic system was developed and performed on human cadavers and deemed exempt by the Mayo Clinic's Institutional Review Board (Supplemental Information) [30]. The specimen group consisted of four male human cadaver heads. MRI imaging was conducted in a SiemensTM (Munich, Germany) Magnetom Prisma 3 Tesla MRI, using the MPRAGE pulse sequence. CT imaging was conducted in a SiemensTM Somatom Definition Flash scanner. The surgical time for device platform placement and both unilateral and bilateral lead implantations were recorded in the last four of five experiments. The device platform placed in experiment 1 was left secured to the cadaveric specimen for experiment 2, and thus only three device platform placement times were recorded. After implantation, the vector error (3D Euclidean distance from the distal end of the first contact to the intended target) and the radial error (shortest 2D difference from the

intended trajectory to the center of the implanted lead) were calculated using the post-operative CT image.

2.9. Surgical planning

COMPASSTM surgical planning software was used to register the MRI and CT images for phantom testing [31]. In addition, it was used for neuronavigation and surgical targeting in the cadaver experiments. The system was additionally tested for its ability to use the MedtronicTM Stealth Station (Medtronic, Inc. Minneapolis, MN, USA).

2.10. System mathematics

The geometry of the D1 stereotactic system can be understood in terms of a cuboid work envelope (100 × 110 × 70 mm) within which lie the main surgical targets and a 'sphere' surrounding it in a manner that the sphere's center may be moved to any target within the work envelope (Arc-centered principle, figure S4). There are six DOF to our frame, the X , Y , Z , collar, arc, and distance. The X is defined as the medial/lateral movement of the frame; the Y is defined as the anterior/posterior movement, and the Z as the superior/inferior movement. The work envelope is at a constant relationship with respect to the device platform placement and the three linear DOF (with the given limits of each inherit in our frame design). This makes it possible to move the center of the sphere to any coordinate within the work envelope and target it with a probe directed normal to the surface of the sphere. The arc and collar angles add angular DOF (trajectory) about the center of the sphere by allowing movement of the probe along two circles lying on the surface of the sphere and oriented along the X – Z and Y – Z planes, respectively. The last DOF, the distance, is the length of the probe along the trajectory, which is kept fixed in our system at 150 mm measured from the top of the device platform to the center of the sphere.

2.11. Statistical analysis

Normality testing was conducted with the Shapiro-Wilks test to determine the proper statistical test. Comparison of mechanical accuracy between the 3D-printed and Delrin[®] systems was performed with an unpaired t -test. Comparison of precision was performed using the F test. Differences in targeting accuracy when manipulating the arc and collar was examined using the Kruskal–Wallis test, and if a significant p value was found Dunn's multiple comparisons test was performed. Comparisons between accuracy of MRI and CT targeting were performed with individual Mann–Whitney tests. Differences in accuracy for targeting different phantom points with both MR and CT was performed using the Kruskal–Wallis test and Dunn's multiple comparisons test if a significant p value was found. Significant effects were set at $p < 0.05$.

3. Results

3.1. Design of the stereotactic system

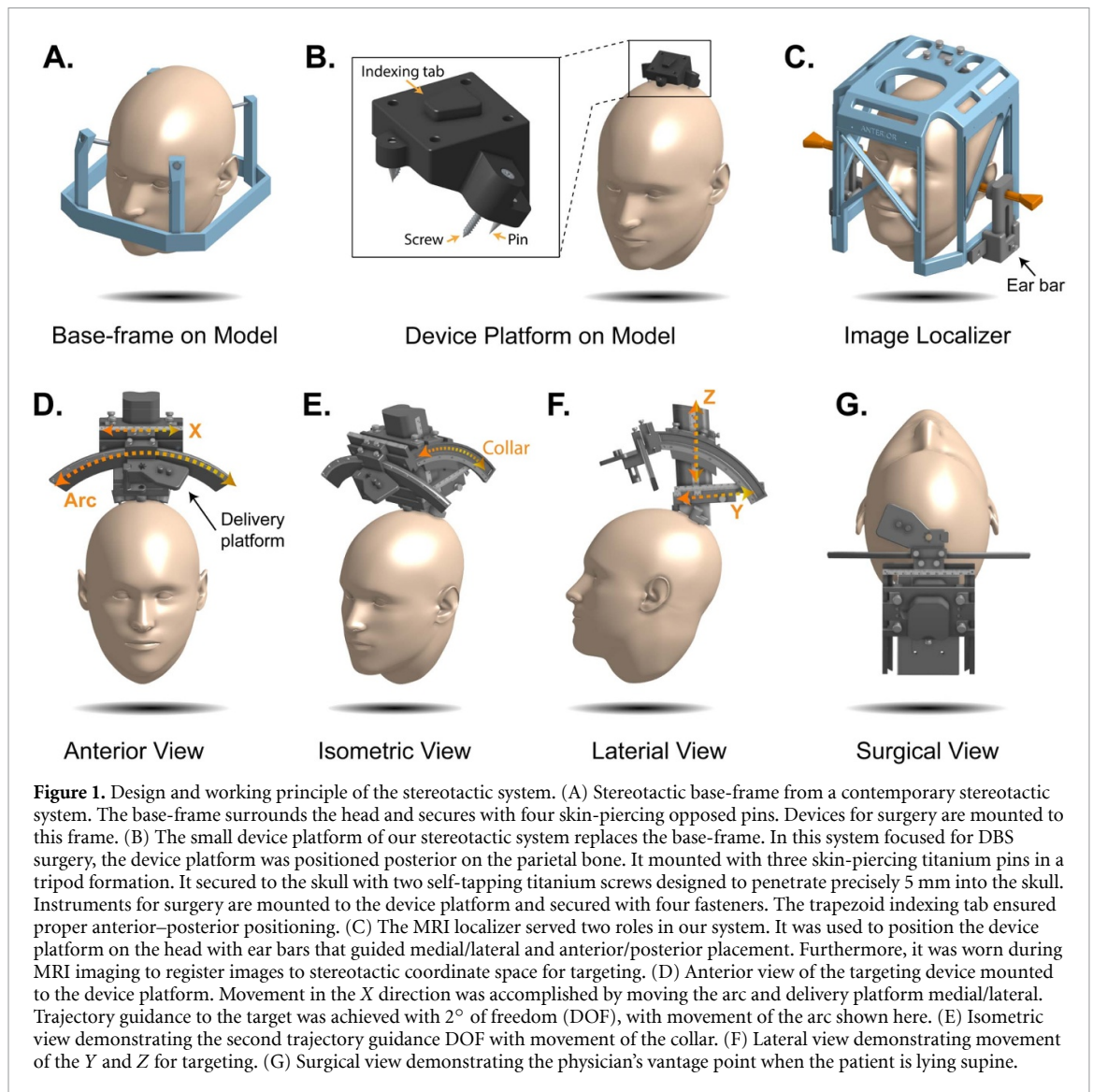
Our design goals included development of a base-frame that was low-profile, magnetic resonance imaging (MRI)-compatible, easily securable to curvilinear bone, and which rigidly remains in place during manipulation of accompanying instrumentation during sequential stages of a procedure. We developed the device platform, which differs from and replaces the classic stereotactic base-frame used in framed systems (figure 1(A)). The dimensions of the device platform were 7.7 cm W \times 5.4 cm L \times 3.8 cm posterior H \times 1.4 cm anterior H with a 30° slope between the anterior and posterior faces (figure 1(B)). The platform mounted to the bone with three skin-piercing titanium stand-off pins and secured with two titanium self-tapping screws. The tripod layout allowed for dispersion of the device weight over the extent of the platform, while the angled design ensured stable contact with curvilinear surfaces. We designed the pins to ensure that they pierced skin and contacted bone while maintaining a skin-platform gap to avoid tissue strangulation [32]. The two self-tapping screws were inserted into laterally placed legs (figure S1(A)) and secured the platform to bone with 5 mm of bone penetration. To ensure that the small footprint of the platform would be able to withstand the weight of the targeting device without failing or causing pain to the patient from rotational forces, we performed torque testing by emulating the force the targeting device would subject to the device platform at the most extreme angle (90°, as if the patient was lying completely supine, see Methods and figures S2(A)). The results of these tests indicated that the device platform could withstand displacement forces at 1x (1.57 Nm) and 3x (4.71 Nm) load when the device platform was perpendicular to gravity (Δ position: $0.76 \pm 2.34 \mu\text{m}$, $2.15 \pm 2.74 \mu\text{m}$; $n = 3$ tests; figure S2). Adjustment of the pin and screw lengths can vary depending on the desired placement location. Previous anatomic studies have reported average skull thickness in the parietal region to be 6 mm; therefore, we chose 10 mm pins and 32 mm screws for use in our device platform [33]. We chose to include a trapezoid indexing tab within the superior portion of the platform to allow for proper and straightforward anterior-posterior positioning of devices (figure 1(B)). We used four fasteners to accomplish accessory device attachment and detachment as needed.

The image localizer was designed to allow image registration to the inherent stereotactic coordinate system (figure S3). The localizer devised here utilized an N-Bar fiducial design typical to frame-based systems (figure 1(C)). Procedurally, it also served as a guide for correct orientation and placement of the device platform on the superior portion of the head. This was accomplished via bilateral adjustable

ear bars that had movement in the X, Y, and Z planes with linear scales (ear bars removed for imaging, see Supplemental Information; figure 1(C)). We developed two interchangeable fiducial compositions for image registration: a 2 mm diameter tube containing 2% CuSO₄ solution in water for MRI imaging, and 2 mm diameter copper rods for computed tomography (CT) (figures S4(A)–(D)). Additionally, we designed a cradle to ensure that the localizer laid orthogonal to the scanner bore (figure S4(E)). Commercial planning software performed MRI image registration and generated an interface for successful selection of target coordinates (X_T , Y_T , Z_T) and the surgical trajectory (C_T , A_T) [31].

We developed our design parameters of the targeting device using the center-of-arc principle to deliver intervention to a wide range of anatomical targets defined in 3D stereotactic space (X, Y, Z) with an adjustable trajectory (semicircular arc and collar, figures 1(D) and (E), movie S1) [34]. The coordinate system was similar to that of frame-based systems, with the origin on the right, posterior, and superior aspect of the head [19]. For implantation, the probe (outer cannula, biopsy needle, etc) projected a path to the center (focus) of the arc-quadrant along its normal vector. Manipulation of the two degrees of freedom (DOF) of the arc-quadrant, the arc and collar angles, allowed the device to approach the target from a multitude of directions (figure S3). Linear medial/lateral, anterior/posterior, and superior/inferior adjustments moved the focus to the surgical target (figures 1(D) and (F), movie S1). Angular scales allowed for arc and collar manipulation $\pm 1^\circ$, and Vernier scales allowed X, Y, and Z movement to ± 0.1 mm. Thumb screw-actuated brakes secured the chosen targeting and trajectory values. Figure 1(G) demonstrates the surgical view after targeting device attachment while the patient lies supine on the operating table. X-ray reticles were attached intra-operatively to the targeting device for assessment of probe position (figure S5). The device's delivery platform allowed for attachment of commercial microdrives for controlled descent and ascent of instrumentation (e.g. DBS electrodes) into the brain.

To demonstrate the robustness of our system when fabricated with low cost materials, we simultaneously developed a single use 3D-printed system and a conventionally manufactured repeated use system. Tough polylactic acid was chosen for 3D-printing as it has considerable tensile strength and stiffness, is resistant to warping, and has high post-printing machinability. We chose Delrin[®] acetal homopolymer (DuPont, Wilmington, DE) for the repeated use system as it has a high strength-to-weight ratio, high-wear resistance, maintains dimensional stability, is low-friction, and can be sterilized. These material qualities are ideal for use in a stereotactic system that requires tight-tolerances and smooth part

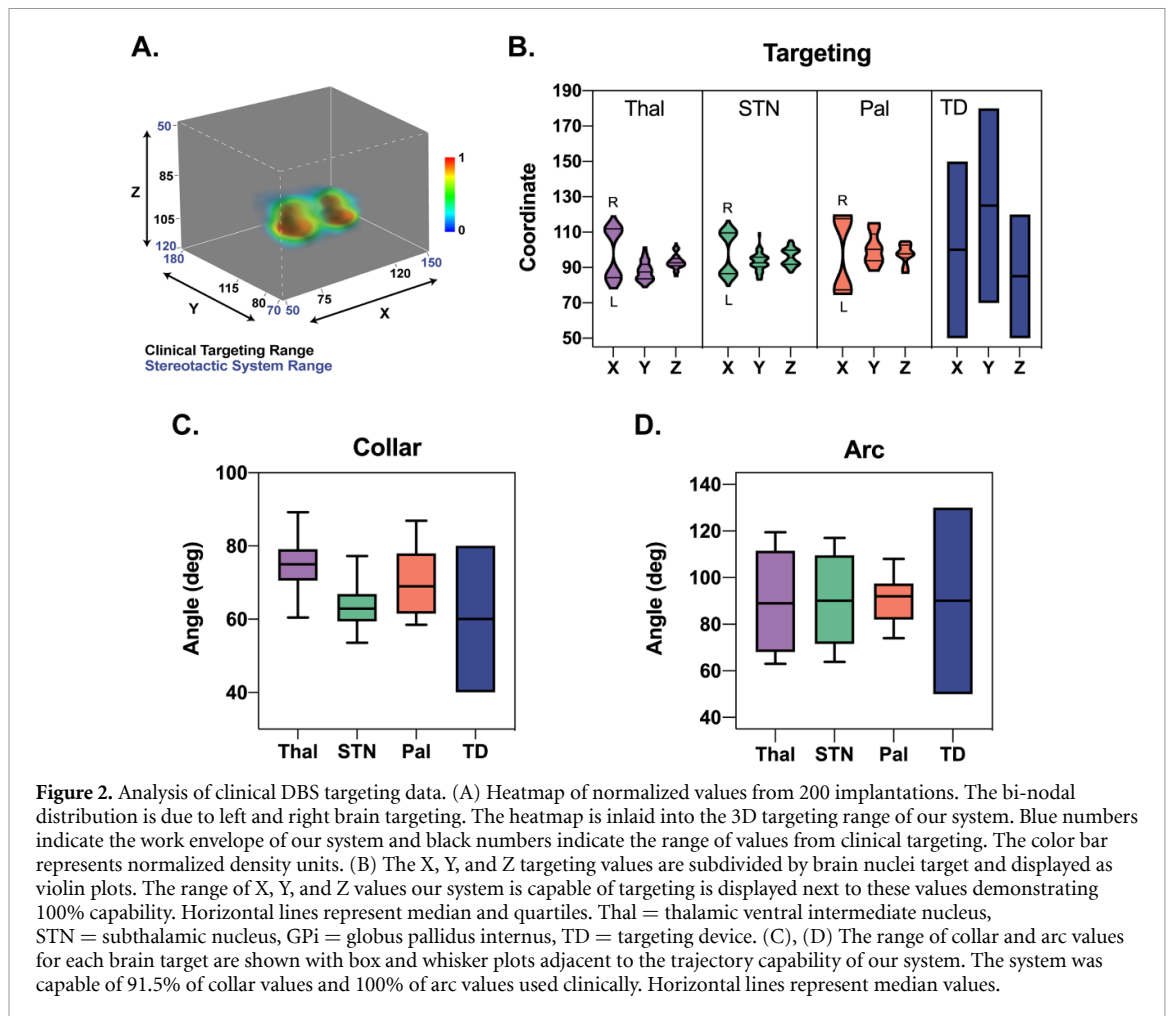


interfaces to maintain accuracy and reliability. The weight of the 3D-printed and Delrin® device platforms were 0.055 kg and 0.091 kg, respectively. The 3D-printed and Delrin® targeting devices weighed 0.635 kg (1.4 lbs) and 0.962 kg (2.2 lbs), respectively, significantly lower than clinical frame-based systems [27].

3.2. Refinement of the targeting device using clinical DBS targeting data

We aimed to demonstrate the versatility of our design principles and refined our system's targeting and trajectory capabilities to align with those used in DBS surgery. To do so, we analyzed 100 patients who underwent bilateral electrode implantation for surgical targeting and trajectory values (total implantations = 200). Of the 100 patients, 37 patients had thalamic ventral intermediate nucleus (Thal) implantations for essential tremor, 56 underwent subthalamic nucleus implantations (STN) for Parkinson's disease, and 7 underwent globus

pallidus internus (GPi) implantations for either disease from 2015 to 2018 at the Mayo Clinic by the same neurosurgeon. After normalizing all values to a reference patient and transforming these values to our system's coordinate system, we calculated the adjusted X, Y, and Z targeting values and collar and arc trajectory values for each brain target (figure 2, table S1) [19]. The range of X, Y, and Z from all targets were 75.1–119.4 mm, 79–115.1 mm, and 85.2–105.4 mm from the origin, respectively (figures 2(A), (B) and S6(A)). To test our device's performance at clinically-relevant ranges capable of hitting all DBS targets, we adjusted our X, Y, and Z ranges to 50–150 mm, 70–180 mm, and 50–120 mm, respectively (figures 2(A) and (B)). The ranges of collar and arc values were 53.6–89.2° and 63–119.5°, respectively (figures 2(C), (B) and S6(B), (C)). Our system achieved a collar range of 40–80° and an arc range of 50–130°, capable of targeting 91.5% of collar values (table S1, 183/200 Total, 59/74 Thal, 112/112 STN, 12/14 Pal) and 100% of arc values (figures 2(C) and (D)).



3.3. Characterization of system accuracy

We first sought to examine the accuracy of our system *ex vivo*. The average mechanical error for the 3D-printed system was found to be 1.4 ± 0.05 mm across 5 target points on a calibrated testing platform (figures 3(A) and (B), $n = 3$ examiners). The Delrin® system had a mechanical error of 0.62 ± 0.05 mm (figure 3(B), $n = 3$ examiners). The 3D-printed and Delrin® frames were compared for accuracy and the Delrin® device displayed significantly reduced error and increased precision on average (pooled data, unpaired *t*-test, $p < 0.0001$, F test, $p = 0.001$), but not at individual points (figure 3(B), multiple individual Mann-Whitney tests, $p > 0.05$ for all points). Next, we assessed whether targeting error was affected when the trajectory angle was manipulated, as varying angles can increase torque on the system. For the 3D-printed system, we varied the collar angle which resulted in an average Euclidean error of 1.2 ± 0.12 mm (figure S7(A), $n = 3$ examiners for each of five angles) and varied the arc angle which resulted in an average Euclidean error of 1.06 ± 0.11 mm (figure S7(B), $n = 3$ examiners or each of nine angles). There was no significant contribution to error as either collar or arc were adjusted to their extreme values (Kruskal-Wallis test, arc: $p = 0.70$, collar: $p = 0.77$). For the Delrin®

system, the average Euclidean distance for different collar and arc angles was found to be 0.62 ± 0.06 mm and 0.78 ± 0.04 mm, respectively (figure S7, $n = 3$ examiners). Similar to findings from the 3D-printed system, there was no statistically significant difference in error between all arc and collar angles assessed (Kruskal-Wallis test, Arc: $p = 0.35$, Collar: $p = 0.004$, Dunn's multiple comparisons test $p > 0.05$ for all comparisons).

We conducted phantom testing to determine the error contributed by imaging and image registration (figures 3(C) and (D)). The target registration error (TRE), the vector error in selecting a target after image registration, was 1.45 ± 1.07 (geometric mean \pm geometric SD) for the CT localizer, and 1.53 ± 1.07 for the MRI localizer when averaged across all 8 phantom targets (figures 3(E) and S8(A)). TRE did not differ between imaging modalities (Mann-Whitney test, $p > 0.05$). However, CT had significantly more variation in TRE across points (F Test, $p = 0.0005$). We then assessed the combined error from imaging and our targeting device. Using the 3D-printed frame, the average targeting error (vector error) between the MRI-targeted and frame-targeted coordinates was 1.79 ± 0.41 mm (figures 3(F) and S8(B)). This was close to the

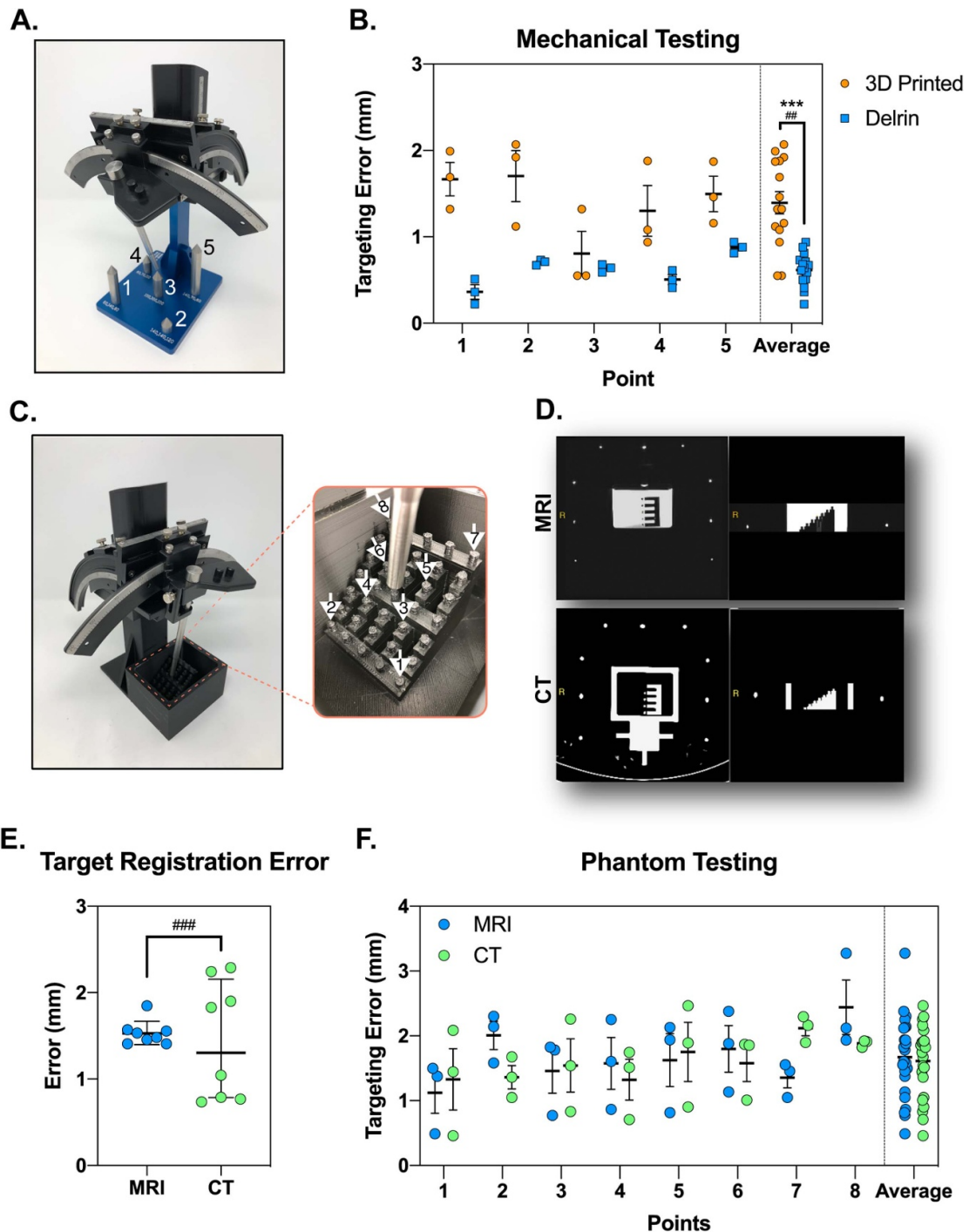


Figure 3. Mechanical and imaging accuracy assessment of the stereotactic system. (A) The targeting device mounted on the mechanical accuracy testing platform. A 150 mm probe (radius of the arc and collar) was used to target each one of the five test points. (B) Mechanical testing of the 3D-printed and Delrin[®] fabricated system was performed, demonstrating robust millimetric accuracy of both systems. The Delrin[®] system was significantly more accurate and precise than the 3D-printed system on average (pooled data, *Mann-Whitney and *F Test). (C) Error introduced from MR and CT imaging modalities was assessed by mounting the targeting device to a custom-built phantom and recording the X, Y, and Z readout from eight points. (D) The phantom was then imaged in both MRI and CT scanners with the respective localizers attached. Image registration was performed using COMPASS[™] software. (E) The average target registration error across points for both CT and MRI imaging was calculated, and MRI values had increased precision (*F Test). (F) The error between image-targeted and frame-targeted were calculated for each point in both imaging modalities. Each test was conducted by three independent examiners. Horizontal bars represent mean values and whiskers are SEM. ## $p < 0.01$, ***/### $p < 0.001$.

limit of true error detection, which is the voxel size of MPRAGE MRI images used in these tests (0.8 mm^3). The average vector error between the frame-targeted and the CT-targeted coordinates was

$1.72 \pm 0.39 \text{ mm}$ (figures 3(F) and S8(B)). MRI and CT data sets achieved similar accuracy when used to target spatially distinct points (Kruskal–Wallis test, CT: $p = 0.31$; MRI: $p = 0.23$). These results

demonstrate that our system is capable of achieving high fidelity image-guided targeting across varying targets and trajectories.

3.4. Clinical performance validation

We next performed mock-surgeries on human cadavers to assess the biomechanical stability of the device platform, determine the stereotactic system accuracy in the context of implanting a DBS electrode, and evaluate the clinical workflow. The device platform effectively secured to bone with easy positioning using the MRI localizer (figure 4(A)). The adjustable ear bars allowed for midline positioning with minimal pitch, yaw, and roll. The MRI localizer enabled successful 3 T MRI image registration for stereotactic neuronavigation using commercial software (figures 4(B) and (C)). After target and trajectory planning, we attached the targeting device with set X_T , Y_T , Z_T , C_T and A_T values to the skull-mounted device platform (figure 4(D)). Once the burr hole location was marked, we quickly removed the targeting device by disengaging the Y break, with the Y rail left in place, for ample surgical access to incise the scalp and drill the burr hole (figure 4(E)). Thereafter, we re-attached the targeting device and set the Y_T value for DBS electrode implantation using an Alpha Omega NeuroNavTM drive (Alpha Omega, Nazareth, Israel) mounted to the stereotactic device (figure 4(F)). We implanted the electrode and secured it to the skull with a StimlocTM anchoring device (Medtronic, MN, USA) (figure 4(G)). We used x-ray reticles for intra-operative confirmation of electrode position and made minor adjustments along the delivery path as needed (figure S5). Once the electrode position was finalized, we evaluated the stereotactic system accuracy (vector/target and radial errors). To do so, we used the CT localizer for CT imaging and registered the images to compare the final electrode position to the planned target position (figure 4(H)). In addition, we used CT imaging to post-operatively assess screw depth and observed no skull penetrations (5.5 mm mean penetration) (figure S1(B)).

Ten DBS implantations into the thalamic ventral intermediate nucleus (VIM) were conducted across five mock surgical experiments using four different cadaveric specimens to assess clinical accuracy and reliability, as well as examine the system's ability to secure to heterogeneous head sizes (figure 5(A)). Figure 5(B) shows post-operative CT imaging from one representative experiment with the pre-surgical plan overlaid onto a post-operative CT scan. After workflow validation was achieved in the initial surgical experiment, the average time to complete three different stages of the surgery was recorded in subsequent experiments (figure 5(C), see Materials and Methods). Device placement took 16.3 ± 2.0 min ($n = 3$), unilateral DBS electrode implantation took 39.1 ± 2.3 mins ($n = 8$) and bilateral DBS electrode

implantation took 78.3 ± 5.4 mins (figure 5(C), $n = 4$). Results from all experiments using the 3D-printed frame found an average vector error of 1.83 ± 0.15 mm and an average radial error of 1.43 ± 0.33 mm (figures 5(D) and (E), $n = 9$ implantations). Of the ten implantations, one was excluded from analyses due to noted intraoperative failure of the electrode securement device. The planned and targeted values for each experiment are shown in figures S8(C) and (D).

4. Discussion

Here, we developed an ergonomic and adaptable stereotactic system that is designed for ease of use, with a bone-mounted low-profile device platform that enables use of surgical instrumentation. We designed and manufactured 3D-printed and Delrin[®] system variants, successfully engineering the components for reliable connectivity and manipulation. Both versions demonstrated robust mechanical and image-guided accuracy. Human cadaveric experiments validated the 3D-printed stereotactic system's capability to withstand surgical manipulation and to accurately target deep brain structures.

These results demonstrate solutions to challenges faced by current stereotactic systems. First, microtargeting systems such as STarFix and Nexframe have been designed to be lightweight and minimalistic to reduce surgical burden and improve patient satisfaction [21, 23, 35, 36]. To achieve this, they have opted for new and non-traditional stereotactic methods (e.g. ancillary tracking system for Nexframe) that lack the intra-operative targeting flexibility of framed systems, which has limited their adoption [1]. The STarFix system is custom-built for each patient and allows only 2 mm of linear intra-operative target adjustment using the Ben Gun. Similarly, Nexframe is restricted to 3 mm of linear adjustment of the Ben Gun, and is capable of only minor trajectory manipulation. These limitations were central to our design considerations and we engineered our system for expanded movement in all three dimensions, allowing our system to perform bilateral and multifocal implantations without the need for detachment and movement of the device platform. This expanded range of motion confers significant utility for procedures that often require multiple trajectories, such as DBS and stereoelectroencephalography. Second, our targeting device has the ability to set coordinates prior to surgical application, improving speed and efficiency. Third, common complaints among patients wearing frame-based systems are the severe discomfort experienced by the inability to freely move their neck during surgery, the obtrusive nature of the frame due to its size, and the locations of the skull-mounted pins. Our system resolves these criticisms by introducing a skull-mounted design which does not enter the patient's vision, is significantly lighter than

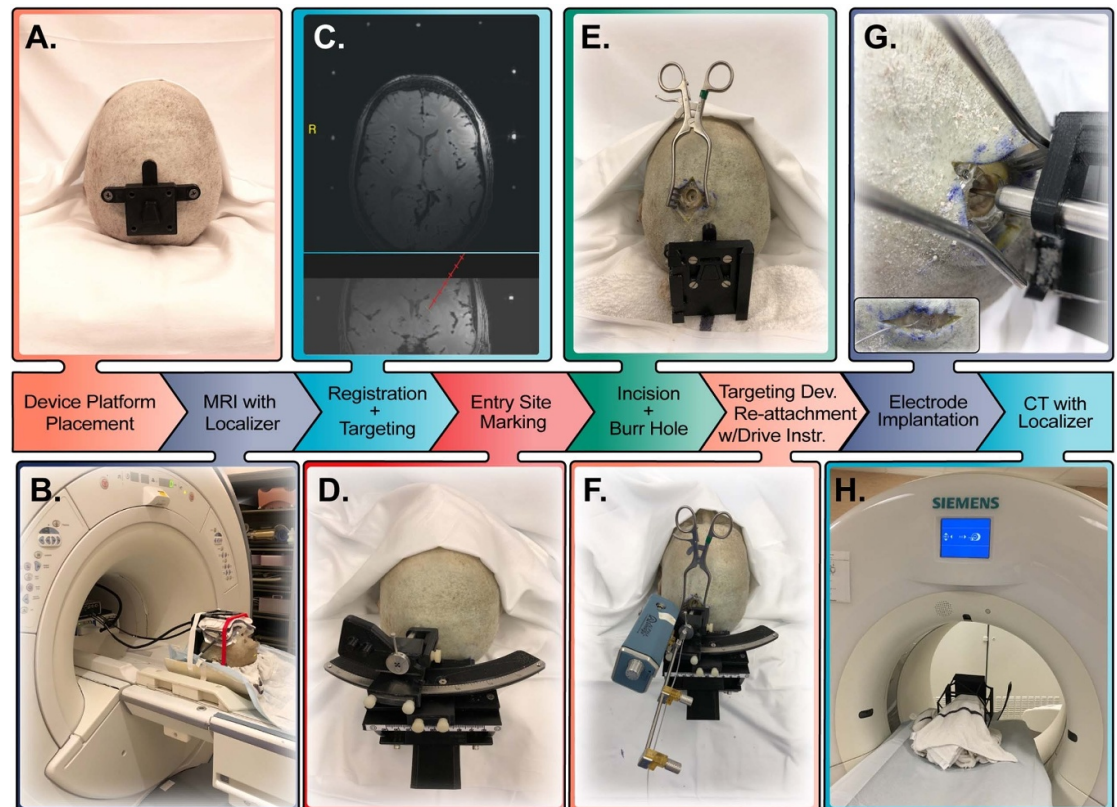


Figure 4. Mock-DBS surgical procedure on a cadaveric specimen. (A) Device platform placement and securement with titanium self-tapping screws. (B) The MRI localizer was mounted to the device platform for 3 T MRI neuroimaging. (C) The Compass™ planning software was used for image registration and target planning. (D) The targeting device was mounted to the device platform to mark the skin (E) for precise burr hole placement. (F) The targeting device was re-attached for DBS electrode delivery using an Alpha Omega NeuroNav™ drive instrument. (G) After the electrode was delivered, the electrode lead was secured to the skull with a Stimloc™ device. (H) After electrode securement, the CT localizer was attached for imaging to determine the final electrode position.

traditional frame-based systems, and does not require the patient to keep their neck stationary during surgery. Fourth, we were able to bilaterally implant electrodes in under three hours, a marked reduction in operating time based on our experience using frame-based systems, as well as those reported from other academic centers [37]. This reduction in operating time markedly reduces the risk of infection and allows for an increased number of cases to be performed in a single operative day. In combination, these advantages will remove several of the deterrents currently inherent to DBS procedures, engendering greater accessibility to restorative neurosurgery.

We demonstrated robust and reproducible accuracy in our clinical system. Performance testing in a simulated operative environment yielded high surgical accuracy with an entirely 3D-printed system. This accuracy is on par with the most accurate results reported for clinical systems (figure S9) [20, 22, 35]. These include results for comparable microtargeting systems like the Nexframe, which has reported clinical accuracy of 1.6–3.2 mm, and STarFix, which has between 2.0 and 2.8 mm accuracy. Additionally, these results are nearly identical to the 1.85 mm error found in a stereotactic system with similar mechanical

principles previously developed by our group [30]. These findings show the important potential for 3D printing in surgical instrumentation and we envision further development of this technology will allow on demand ready-to-use surgical systems [38]. Further, the economical cost of 3D printing offers potential for stereotaxy to spread to developing countries where conventional systems are cost-prohibitive. This would allow safe neurosurgical intervention for patients who would otherwise be unable to receive such care.

There are a number of practical limitations worth noting with the system's current configuration. First, once the device platform is secured to bone and the targeting device is attached, there is a set constraint of the targetable work envelope. The work envelope was optimized here for application to DBS surgery, and retrospective clinical data demonstrated the system's capability of hitting all surgical targets. In addition, the system's design principles allow for expansion or retraction of the targeting range, and minor modification of the system's configuration would enable additional surgical indications. One such modification would address a limitation in systems that are based on the center of arc principle: movement only about the X-Z (arc) and Y-Z (collar) planes [2]. Rotation

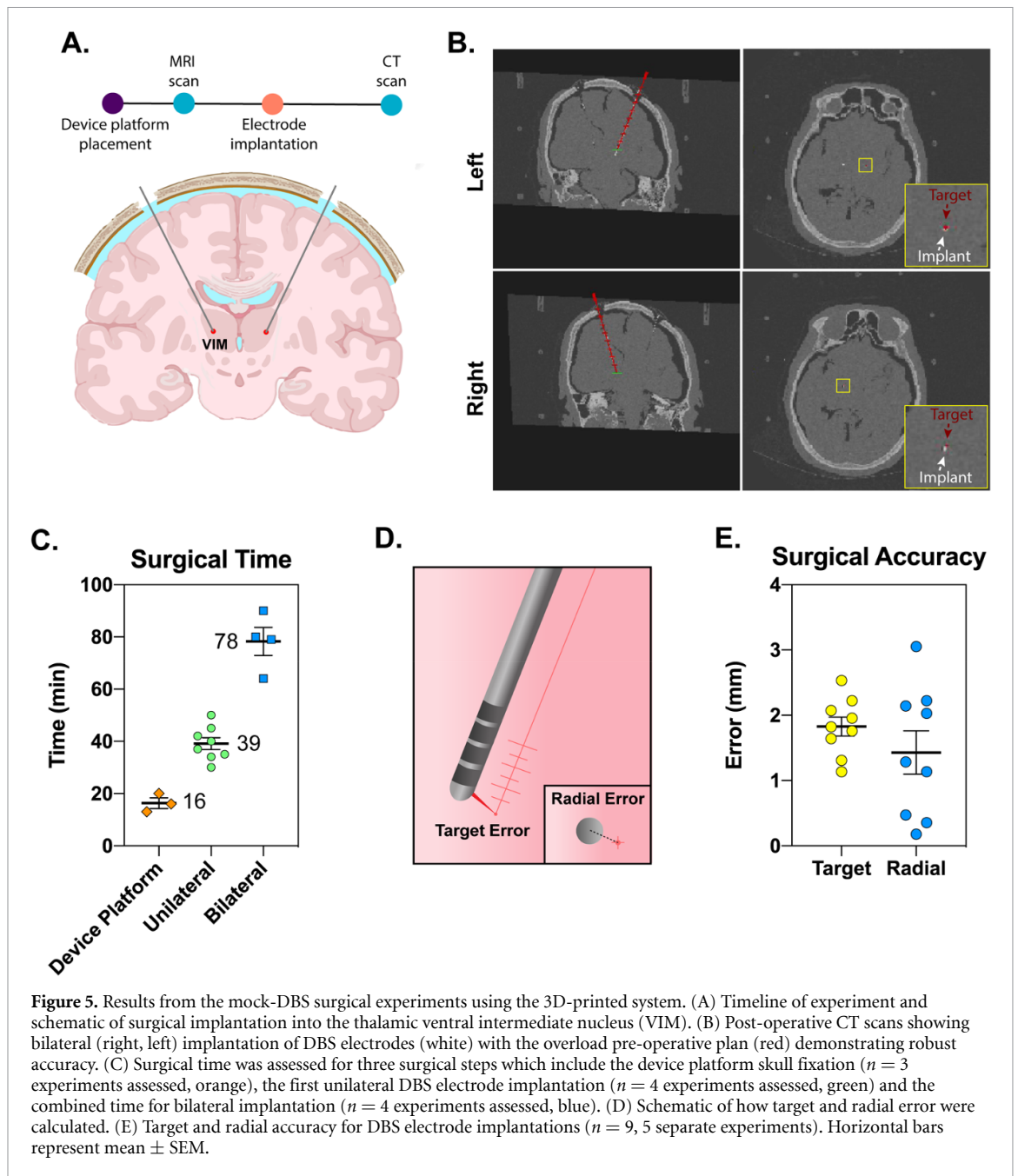


Figure 5. Results from the mock-DBS surgical experiments using the 3D-printed system. (A) Timeline of experiment and schematic of surgical implantation into the thalamic ventral intermediate nucleus (VIM). (B) Post-operative CT scans showing bilateral (right, left) implantation of DBS electrodes (white) with the overload pre-operative plan (red) demonstrating robust accuracy. (C) Surgical time was assessed for three surgical steps which include the device platform skull fixation ($n = 3$ experiments assessed, orange), the first unilateral DBS electrode implantation ($n = 4$ experiments assessed, green) and the combined time for bilateral implantation ($n = 4$ experiments assessed, blue). (D) Schematic of how target and radial error were calculated. (E) Target and radial accuracy for DBS electrode implantations ($n = 9$, 5 separate experiments). Horizontal bars represent mean \pm SEM.

about the X-Y plane can be accomplished in our system by enabling circular movement at the interface of the targeting device and device platform. This would enable circular expansion of the targeting envelope and provide added versatility for multifocal surgical intervention, such as stereoelectroencephalography for treatment of epilepsy [39]. Another limitation to note is that cadaveric experiments were performed without concern for surgical draping and sterility, and this will be necessary prior to clinical translation. Furthermore, the number of tests we performed for usability and accuracy are small compared to the number of application cycles used in clinical practice. Experiments will need to assess long-term reliability including biostability and compatibility with sterilization.

Our system is adaptable to stereotactic guidance beyond treatment of neurologic disorders. This utility is achieved through development and modifications of the small device platform which allows the system to rigidly mount to bone with a small surface area. While the current design scheme was tested for skull placement, it can be readily modified for attachment to surfaces with sufficient area for pin and screw securement. We envision the device platform could be attached to the femur or ribs for stereotactic biopsy and focal treatment, or to the spine for stereotactic radioablation. To our knowledge, this is the only stereotactic system to offer this potential. Thus, this versatile stereotactic system provides a powerful tool for clinical therapeutic and diagnostic applications.

Acknowledgments

We thank Terry Reed of the Mayo Clinic Division of Engineering for his hardware fabrication support, Bruce Kall for his stereotactic software technical support, the Anatomical Services Department for supplying specimens, Alexander Hooke of the Biomechanics Laboratory for help with torque testing, and the Mayo Clinic Center for Advanced Imaging Research for their support.

Author contributions

K H L and S G invented the frame technology. K H L, S J G, Y O and A E R conceptualized the ideas, research goals, and aims. A E R was responsible for methodology, data curation, formal analysis, investigation, data validation, data visualization, and writing of the original draft. K H L, Y O, S G, and C D B contributed to methodology, project administration, study resources, supervision, and manuscript review. All authors contributed to study investigation and manuscript review and editing. K H L and K E B acquired funding.

Conflict of interest

The stereotactic system described in this paper is licensed to NaviNetics Inc. of Rochester, MN through Mayo Clinic Ventures. K E B, S J G, K H L and Mayo Clinic hold stock in NaviNetics Inc. Technology described here are patented under 'Neurosurgical Systems and Related Methods,' World Patent No. WO/2019/157 070.

Data and materials availability

All data associated with this study are present in the paper or the supplementary materials. All data and materials requests for reproducibility studies, data validation, and research use will be reviewed by K H L and Y O.

Funding

This work was funded by a gift from The Grainger Foundation, an NIH T32 Medical Scientist Training Program Grant (GM065841) awarded to K H L and assigned to A E R, and training grants NIH F31NS115202, NIH R25GM055252-23 and NIH TL1R002380-03 assigned to A E R. In addition, A E R would like to acknowledge a Society for Neuroscience Leadership Development Program Award. A S B was funded by a Boston Scientific Fellowship Award.

ORCID iDs

Aaron E Rusheen  <https://orcid.org/0000-0001-8029-1167>

Abhijeet S Barath  <https://orcid.org/0000-0002-7019-5670>

Yoonbae Oh  <https://orcid.org/0000-0003-1779-978X>

References

- [1] Owen C M and Linskey M E 2009 Frame-based stereotaxy in a frameless era: current capabilities, relative role, and the positive- and negative predictive values of blood through the needle *J. Neurooncol.* **93** 139–49
- [2] Leksell L 1951 The stereotaxic method and radiosurgery of the brain *Acta Chir. Scand.* **102** 316–9
- [3] Benabid A L, Pollak P, Hoffmann D, Gervason C, Hommel M, Perret J E, de Rougemont J and Gao D M 1991 Long-term suppression of tremor by chronic stimulation of the ventral intermediate thalamic nucleus *Lancet* **337** 403–6
- [4] Picard C, Olivier A and Bertrand G 1983 The first human stereotaxic apparatus. The contribution of Aubrey Mussen to the field of stereotaxis *J. Neurosurg.* **59** 673–6
- [5] Spiegel E A, Wycis H T, Marks M and Lee A J 1947 Stereotaxic apparatus for operations on the human brain *Science* **106** 349–50
- [6] Horsley V, Clarke R H and Structure T 1908 Functions of the cerebellum examined by a new method *Brain* **31** 45–124
- [7] Leksell L 1971 *Stereotaxis and Radiosurgery; an Operative System* (Thomas, Springfield, Ill.) p xiii, 69
- [8] Ostertag C B, Mennel H D and Kiessling M 1980 Stereotactic biopsy of brain tumors *Surg. Neurol.* **14** 275–83
- [9] Munding F 1985 CT stereotactic biopsy for optimizing the therapy of intracranial processes *Acta Neurochir. Suppl.* **35** 70–74
- [10] Riechert T and Wolff M 1951 A new stereotactic instrument for intracranial placement of electrodes *Arch. Psychiatr. Nervenkr. Z Gesamte Neurol. Psychiatr.* **186** 225–30
- [11] Dandy W E 1918 Ventriculography following the injection of air into the cerebral ventricles *Ann. Surg.* **68** 5–11
- [12] Foote R L et al 2012 The clinical case for proton beam therapy *Radiat. Oncol.* **7** 174
- [13] Dandekar M P, Fenoy A J, Carvalho A F, Soares J C and Quevedo J 2018 Deep brain stimulation for treatment-resistant depression: an integrative review of preclinical and clinical findings and translational implications *Mol. Psychiatry* **23** 1094–112
- [14] Khan F R and Henderson J M 2013 Deep brain stimulation surgical techniques *Handb Clin Neurol* **116** 27–37
- [15] Couldwell W T and Apuzzo M L 1990 Initial experience related to the use of the Cosman-Roberts-Wells stereotactic instrument. Technical note *J. Neurosurg.* **72** 145–8
- [16] Safaee M, Burke J and McDermott M W 2016 Techniques for the application of stereotactic head frames based on a 25-year experience *Cureus* **8** e543
- [17] Brown R A 1979 A computerized tomography-computer graphics approach to stereotaxic localization *J. Neurosurg.* **50** 715–20
- [18] Goerss S, Kelly P J, Kall B and Alker G J Jr. 1982 A computed tomographic stereotactic adaptation system *Neurosurgery* **10** 375–9
- [19] Leksell L, Leksell D and Schwebel J 1985 Stereotaxis and nuclear magnetic resonance *J. Neurol. Neurosurg. Psychiatry* **48** 14–18
- [20] Bjartmarz H and Rehn Crona S 2007 Comparison of accuracy and precision between frame-based and frameless

Q8

Q9

- stereotactic navigation for deep brain stimulation electrode implantation *Stereotactic Funct. Neurosurg.* **85** 235–42
- [21] Kelman C, Ramakrishnan V, Davies A and Holloway K 2010 Analysis of stereotactic accuracy of the cosman-robert-wells frame and nexframe frameless systems in deep brain stimulation surgery *Stereotactic Funct. Neurosurg.* **88** 288–95
- [22] Bot M, van den Munckhof P, Bakay R, Sierens D, Stebbins G and Verhagen Metman L 2015 Analysis of stereotactic accuracy in patients undergoing deep brain stimulation using Nexframe and the Leksell frame *Stereotactic Funct. Neurosurg.* **93** 316–25
- [23] Holloway K L et al 2005 Frameless stereotaxy using bone fiducial markers for deep brain stimulation *J. Neurosurg.* **103** 404–13
- [24] Palys V and Holloway K L 2018 Frameless functional stereotactic approaches *Prog. Neurol. Surg.* **33** 168–86
- [25] Winkler D, Hammer N, Oehlwein C, Schwarz J, Strecker K, Fritsch D and Meixensberger J 2013 Implementing conventional Zamorano Dujovny frames versus individually manufactured microTargeting platforms—a comparative study on deep brain stimulation in Parkinson patients *Stereotactic Funct. Neurosurg.* **91** 392–8
- [26] Tai C H, Wu R-M, Lin C-H, Pan M-K, Chen Y-F, Liu H-M, Lu -H-H, Tsai C-W and Tseng S-H 2010 Deep brain stimulation therapy for Parkinson's disease using frameless stereotaxy: comparison with frame-based surgery *Eur. J. Neurol.* **17** 1377–85
- [27] Elekta 2015 Instructions for use, leksell stereotactic system®
- [28] Ben-Haim S and Falowski S M 2018 Evaluation of patient perspectives toward awake, frame-based deep-brain stimulation surgery *World Neurosurg.* **111** e601–7
- [29] Wang D D, Lau D, Rolston J D, Englot D J, Sneed P K and McDermott M W 2014 Pain experience using conventional versus angled anterior posts during stereotactic head frame placement for radiosurgery *J. Clin. Neurosci.* **21** 1538–42
- [30] Edwards C A et al 2018 A novel re-attachable stereotactic frame for MRI-guided neuronavigation and its validation in a large animal and human cadaver model *J. Neural. Eng.* **15** 066003
- [31] Alterman R L, Kall B, Beric A, Sterio D and Kelly P J 1997 Pallidal targeting with the COMPASS system *Stereotactic Funct. Neurosurg.* **69** 69–72
- [32] Hori H, Moretti G, Rebora A and Crovato F 1972 The thickness of human scalp: normal and bald *J. Invest. Dermatol.* **58** 396–9
- [33] Eisova S, Rangel de Lazaro G, Pisova H, Pereira-Pedro S and Bruner E 2016 Parietal bone thickness and vascular diameters in adult modern humans: a survey on cranial remains *Anat. Rec.* **299** 888–96
- [34] Leksell L 1949 A stereotactic apparatus for intracerebral surgery *Acta Chir. Scand.* **99** 229–33
- [35] Konrad P E, Neimat J S, Yu H, Kao C C, Remple M S, D'Haese P-F and Dawant B M 2011 Customized, miniature rapid-prototype stereotactic frames for use in deep brain stimulator surgery: initial clinical methodology and experience from 263 patients from 2002 to 2008 *Stereotactic Funct. Neurosurg.* **89** 34–41
- [36] Larson P S et al 2012 An optimized system for interventional magnetic resonance imaging-guided stereotactic surgery: preliminary evaluation of targeting accuracy *Neurosurgery* **70** 95–103
- [37] Yin Z, Luo Y, Jin Y, Yu Y, Zheng S, Duan J, Xu R, Zhou D, Hong T and Lu G 2019 Is awake physiological confirmation necessary for DBS treatment of Parkinson's disease today? a comparison of intraoperative imaging, physiology, and physiology imaging-guided DBS in the past decade *Brain Stimul.* **12** 893–900
- [38] Tack P, Victor J, Gemmel P and Annemans L 2016 3D-printing techniques in a medical setting: a systematic literature review *Biomed. Eng. Online* **15** 115
- [39] Gonzalez-Martinez J, Mullin J, Vadera S, Bulacio J, Hughes G, Jones S, Enatsu R and Najm I 2014 Stereotactic placement of depth electrodes in medically intractable epilepsy *J. Neurosurg.* **120** 639–44